The influence of novel beam shapes on melt pool shape and mechanical properties of LPBF produced Al-alloy

Galbusera, F.; Caprio, L.; Previtali, B.; Demir, A. G.

The influence of novel beam shapes on melt pool shape and mechanical properties of LPBF produced Al-alloy

Francesco Galbusera[1], francesco.galbusera@polimi.it

Leonardo Caprio[1], leonardo.caprio@polimi.it

Barbara Previtali[1], barbara.previtali@polimi.it

Ali Gökhan Demir[1]*, aligokhan.demir@polimi.it

[1]Department of Mechanical Engineering, Politecnico di Milano, Via La Masa 1, I-20156 Milan, Italy

*Corresponding author

The influence of novel beam shapes on melt pool shape and mechanical properties of LPBF produced Al-alloy

Francesco Galbusera[1], Leonardo Caprio[1], Barbara Previtali[1], Ali Gökhan Demir[1]*

[1]Department of Mechanical Engineering, Politecnico di Milano, Via La Masa 1, 20156 Milan, Italy

Abstract

New generation of multi-core fiber laser sources provide in-source dynamic beam shaping. Such sources can switch between Gaussian and ring beam profiles, providing new irradiance profiles. The new irradiance profiles add up to the process flexibility for controlling the temperature fields generated in the laser powder bed fusion (LPBF) process. On the other hand, they bring further complexity as new process parameters should be defined and their influence on the mechanical properties unveiled. Accordingly, this work studies the use of seven different beam indexes provided by a multi-core industrial fiber laser source with beam diameters varying between 47 µm to 144 µm during the LPBF of AlSi7Mg0.6 alloy. The beam spatial profiles were measured and descriptive irradiance parameters were defined. The Al-alloy constituted a challenging material type due to its high reflectivity and low melting point, hence, more prone to lack-of-fusion and keyhole defects. LPBF experiments were conducted at fixed energy density and peak irradiance levels investigating the influence of the beam shapes on the melt pool geometry in prismatic samples. The results showed that the peak irradiance and the ring intensity had a direct impact on the melt pool aspect ratio (AR) and melt pool depth to layer thickness ratio (h/z). With all the conditions providing adequately dense parts (>99.5%), the mechanical properties were found to be correlated to the melt pool geometry. The results confirm that the beam shape can be tuned between the central peak and the ring to further manipulate the material properties in LPBF.

Keywords: Beam shaping; Irradiance profile; Non-Gaussian beams; Ring beams; Laser Powder Bed Fusion; Additive Manufacturing

Nomenclature

Symbol	Name	Units
AR	Melt pool aspect ratio	non-dimensional
BS	Beam shape index	non-dimensional
d_0	Beam waist diameter	μm
E	Elastic modulus	GPa
h	Melt pool depth	μm
h_d	Hatch distance	μm
I	Irradiance	W/cm^2
$I_{0,a}$	Average irradiance of the Gaussian profile	W/cm^2
$I_{0,g}$	Peak irradiance of the Gaussian profile	W/cm^2
I_{peak}	Peak irradiance	W/cm^2
P	Laser power	W
UTS	Ultimate tensile strength	MPa
v	Scan speed	mm/s
VED	Volumetric energy density	J/mm^3
w	Melt pool width	μm
YS	Yield stress	MPa
z	Layer thickness	μm
ε_f	Elongation at fracture	non-dimensional
ρ	Density	non-dimensional

1 Introduction

Fiber lasers are arguably the industrially standard sources in Laser Powder Bed Fusion (LPBF). These sources have been amongst the drivers for the wider diffusion of the LPBF technology due to their small footprint, high energy efficiency, and long-term reliability. Commonly, standard single mode fiber laser sources are employed, which provide beams with a Gaussian-like distribution. The single mode fiber lasers provide with high beam quality ($M^2 \cong 1$) which allows to obtain spot sizes typically in the range of 40-100 μm in the scanning area, often with the possibility of enlarging the beam without significantly altering the power distribution. The beam intensity profile is more commonly varied in time by employing continuous (CW) or pulsed wave (PW) emission modes in LPBF systems [1]. For many years, Gaussian beam profile has been a standard in the LPBF technology, but also in laser welding and cutting, where higher power levels are required [2]. However, current advancements in the fiber laser technology provide the possibility of combining Gaussian beams with high beam quality and thus elevated focusability with non-gaussian beam distributions. The recent introduction of multiple-core fiber laser sources in the industry offers novel processing capabilities by in-source dynamic beam shaping in many fields including LPBF which are yet to be explored.

With beam shaping, multiple techniques based on the irradiance distribution manipulation are addressed. In a most generic approach, beam shaping approaches can be divided to static and dynamic methods. Static beam shaping techniques entail the use of static optical elements such as lenses or diffractive optics [3,4] to provide a non-Gaussian beam shape that is not variable throughout the process [5]. Dynamic beam shaping refers to optical elements that can be addressed to manipulate the beam shape. Some of the known approaches are based on the use of spatial light modulators [6], diode arrays [7], and deformable mirrors [8]. The advantages of beam shaping with static methods have been demonstrated for manipulating the melt pool shape in laser welding [9]. Fiber lasers with non-Gaussian beam shapes have also been employed for material processing, which can be grouped under static beam shaping [10]. On the other hand, only recently fiber lasers with programmable in-source dynamic beam shaping capabilities have been introduced to the industrial use [11] with an initial emphasis on laser welding applications [12–14].

With regards to the LPBF process, most of the literature works are focused on static beam shaping methods. Roehling et al. [15], Matthews et al. [16] and Shi et al. [17] showed that elliptical beam profile can induce the

formation of small equiaxed grains of random orientation with LPBF of AISI 316L if compared with a standard gaussian beam. Recently, Tumkur et al. [18] investigated the effect of nondiffractive Bessel beams in the manufacturing of AISI 316L. The authors observed an improvement of density, surface roughness and robust tensile properties as an effect of Bessel beam distribution, capable of stabilizing the melt pool turbulence while reducing thermal gradients and keyhole formation. Cloots et al. [19] observed a reduction of the hot cracking susceptibility of IN738LC when exploiting doughnut profile of irradiance instead of a gaussian one. Wischeropp et al. [20] investigated the effect of the laser beam profile, either gaussian or doughnut, in the LPBF of AlSi10Mg. The authors found that the use of a doughnut beam profile enlarges the processing window along with fewer defects, such as cracks, protrusions and porosity. Improvement of build rate was also shown experimentally by Schleifenbaum et al. [21] with a stainless steel and a tool steel (1.4404 and 1.2343). Other studies focused on the influence of non – gaussian beams, such as top – hat and doughnut profiles. Zhirnov et al. [22] and Metel et al. [23] showed significant improvement on the process stability with non – gaussian beams (top – hat and doughnut profiles) in terms of power and scan speed. Okunkova et al. [24] observed a reduction of the free–of–powder consolidation zone when adopting a doughnut profile instead of a Gaussian profile. Liu et al. [25] obtained different melt pool morphologies, microstructure, crystallographic texture and tensile properties when using top-hat profile with AlSi10Mg. The use of flat – top beams was attempted also by Tenbrock et al. [10], resulting a more uniform temperature distribution while keeping highly – dense structures at moderate energy intensities, and by Loh et al. [26], demonstrating an improvement of build rate. Only recently, in-source dynamic beam shaping has been applied to LPBF process with fundamental single track consolidation studies. Grünewald et al. [27] investigated single tracks of AISI316L, demonstrating a potential increase of processing window for ring shaped profiles enhancing productivity. The same group has recently demonstrated the influence of such beam shapes on the densification of prismatic samples[28]. All works concerning static and dynamic beam shaping means suggest a direct influence of the beam profile on the thermal field and hence, the melt pool characteristics. On the other hand, a systematic investigation on the link between the beam shape, melt pool geometry, and the mechanical properties still requires to be established. For such purpose, in-source dynamic laser beam shaping should be assessed also in multiple layered parts producing 3D objects. To the authors' knowledge, the LPBF of freestanding 3D components with novel beam shapes and material properties of consolidated parts have not yet been reported. Although lasers with in-source

dynamic beam shaping have been introduced to the market [29], evidently the influence of the beam shapes on the melt pool geometry and resultantly the mechanical properties are yet to be understood. Some of the reasons behind the lack of such investigations may be attributed to the integration of these laser sources to open LPBF machines and beam analysis requirements.

Accordingly, the present paper studies LPBF with different irradiance distributions, from gaussian towards ring, provided by a novel high brilliance fiber laser source with in-source beam shaping capability. An industrial laser with in-source dynamic beam shaping was integrated to an open LPBF machine and the beam profiles were characterized. With the developed system LPBF alloy AlSi7Mg0.6 with different beam profiles was investigated [30]. The chosen Al-alloy is from an alloy family with known LPBF processability, while posing difficulties due to its high optical reflectivity, high affinity to oxidation, and low melting point rendering the process difficult [31]. Moreover, these alloys often require multiple heat treatment stages to relieve the residual stresses and retain the mechanical properties [32]. Indeed, a large margin of process regulation can be foreseen concerning several applications in the aerospace and automotive fields. The paper systematically shows the analysis of the beam characteristics and their influence on the melt pool geometry. The work provides a link between the irradiance parameters and the melt pool geometry characteristics, which control the mechanical properties.

2 Melt pool shape manipulation through the laser beam shape

The melt pool shape depends on the thermal field generated by the laser beam. Indeed, the beam intensity profile changes the temperature distribution within the melt pool, where the highest temperatures are generated naturally around the peak intensity. With increased intensity, the fraction of vapour generated on the melt pool surface may increase changing also the recoil pressure applied on the melt pool. With increased recoil pressure, the processing conditions may move from conduction to an intermediate phase to finally the keyhole mode [33]. Often in LPBF, Gaussian-like beam distributions are used. Inherently, the temperature distribution is expected to be steeply decaying from the centre of the beam towards the outer regions, with an intense vaporization front starting at the beam centre. Although the stability of the melt pool over the single track is the main block for process stability, processing conditions in LPBF are often discussed as a function of the volumetric energy density (E) expressed as [34]:

$$VED = \frac{P}{vzh_d} \tag{1}$$

where P is the laser power, v is the scan speed, z is the layer thickness and h_d is the hatch distance. The volumetric energy distribution neglects the influence of the beam intensity profile. For Gaussian-like beam distributions the intensity if commonly discussed as the average irradiance ($I_{a,g}$) and the peak irradiance ($I_{0,g}$), which can be defined as follows:

$$I_{a,g} = \frac{4P}{d_s^2 \pi} \tag{2}$$

$$I_{0,g} = \frac{8P}{d_s^2 \pi} \tag{3}$$

where d_s is the beam diameter at $1/e^2$ intensity. The average beam irradiance corresponds the average intensity of the beam, which is a convenient parameter where the beam distribution may not be easily determined as Gaussian-like. Such conditions were more relevant especially with older generation of CO_2 and Nd:YAG lasers with high M^2 values producing laser beams composed of high order of TEM (transverse electromagnetic mode) [35]. The peak irradiance corresponds to the peak intensity in the beam centre. It is easily calculated for a Gaussian beam with a hypothesis that the beam intensity integral can be taken equal to a uniform distribution between $-2d_s/\sqrt{2}$ and $2d_s/\sqrt{2}$ [36]. The average irradiance is more commonly used for laser welding applications, where the process commonly does not require consecutive overlapped tracks [37]. The peak irradiance is widely used in laser micromachining applications to estimate ablation threshold of materials [38] or to investigate the process quality [39]. While all attempts to define a complex laser beam with a single parameter is likely to miss essential information, the addition of an irradiance parameter to LPBF process studies is relevant especially considering non-conventional beam shapes. Indeed, the new generation active fiber lasers with in-source dynamic beam shaping capabilities require further attention from this perspective. A flat beam shape or ring beam modes achievable via the new generation active fiber lasers could allow for a different and possibly a more homogenous temperature distribution and a larger melt pool width (*w*) without necessarily varying the volumetric energy density. However, the redistribution of the beam intensity profile with a reduction of the peak and an increase towards the tails can reduce the penetration depth (*h*). Such beam shapes are achievable with double-core fiber laser systems providing in-source beam shaping capabilities. The different beam shapes are expected to redistribute also the melt pool shape. The variation of the melt pool shape also determines the *h/z* ratio, indicative of how well the melted layer adheres to the previous ones.

Accordingly, the experimental study was conducted to reveal the influence of the beam shape and hence the irradiance profile on the melt pool geometry.

3 Materials and methods

3.1 LPBF system

An industrial LPBF system with open architecture (3D-NT LLA150R, Solbiate Olona, Italy) was used throughout this work. The system was equipped with a double-core fiber laser source with in-source beam shaping capabilities (nLIGHT AFX 1000, nLIGHT Inc, Vancouver, Washington, USA). The laser emitted at a wavelength of 1070 nm (±10 nm), with a maximum power of 600 W using the central single mode core and of 1200 W when the outer ring is also employed. The optical chain used for the laser beam delivery comprises a collimating lens (OPI Photonics, Torino, Italy) with a focal length of 60 mm, a beam expander unit with an expansion factor of 1.25, a scanner head (Raylase MS-III, Raylase, Weßling, Germany) and an f-theta lens with a focal length of 254 mm (Ronar, Qioptiq, Waltham, US). The calculated beam waist diameter in the focus position is 47 μm when the central single-mode core is employed producing a Gaussian-like power distribution. The LPBF system was controlled with a tailor made control software allowing to control beam parameters down to the scan vector level (Direct Machining Control, Vilnius, Lithuania). During building, oxygen content was kept under the threshold of 0.3% by purging and filling the chamber with Ar in overpressure.
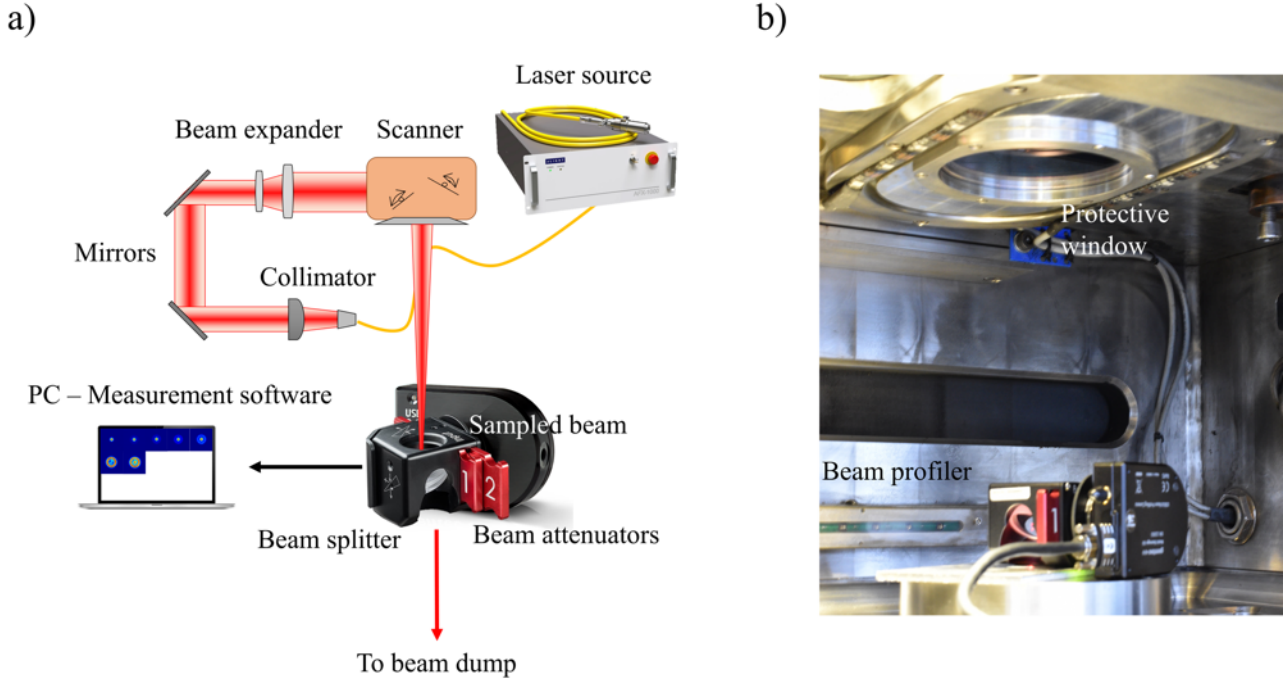
Figure 1: a) Schematic view of the optical chain of the LPBF system and the beam measurement setup. b) Beam profiler installed in the chamber LPBF system.

The employed novel laser with in-source beam shaping capabilities had seven programmable spatial beam profiles. A distinction between the spatial profiles can be made according to the power distribution between the central core and the outer ring of the fiber. As the power is distributed between the central core and the outer ring of the fiber, the beam profile shifts from gaussian towards a ring profile. In this work, different beam shapes are referred to with an index namely BSi, where i ranges from 0 for the gaussian and 6 for the doughnut with the highest power distributed over the tails. Table 1 shows the power ratios between the ring and the core of the beam as declared by the producer [29]. The beam shapes were characterized employing a beam profiler (Gentec Beamage Series USB 3.0, Quebec City, Canada) based on a CMOS camera. The beam was sampled through a beam splitter and attenuators as seen in Figure 1. The caustic shape of each profile was also reconstructed by acquiring the beam distribution along its propagation path in z with a $\Delta z = 0.25$ mm distance between the acquisition points. The measurements were carried out according to ISO11146 and ISO11670 standards, calculating beam waist diameter (d_0), beam quality factor (M^2), and beam divergence (θ). The beam shape measurements were carried out in the central part of the F-theta lens. The stability of the beam was verified with linear marking experiments in the scan field. Beam waist diameters (d_0) measured at $1/e^2$ level in the focus position were comprised between 49 μm for the Gaussian-like mode (BS0), and 144 μm for the

9

doughnut profile (BS6) as shown in Table 1. Laser power was characterized by a power meter (W-3000-D55-SHC, Laserpoint, Vimodrone, Italy).

Figure 2.a displays the caustic shape propagation of the different beam shapes whilst Figure 2.b shows the irradiance profiles of the employed beam shapes in terms of I/I_{max}, where I_{max} represents the irradiance peak of the Gaussian-like profile measured at 200 W laser power. It can be seen that as the beam index is increased the beam becomes larger and the main central irradiance peak is reduced gradually. At higher beam indexes (BS4 to BS6) the irradiance levels at the ring become higher moving towards the ring shaped profiles. The beam shapes were also categorized in terms of the closest TEM assignable to them [35]. Considering a Laguerre–Gaussian distribution the values are given in TEM_{pl} where p refers to the number of radial zero fields and l is the number of angular zero fields. The indexes BS0 and BS1 are found to be close to a Gaussian beam, which were considered as TEM_{00}. The defined Laguerre–Gaussian distributions are only a close representation of the beam shapes since the irradiance profiles might differ from their analytical definition. For indexes BS2, BS3, and BS4 the beam appears to be split with a central peak and a surrounding ring, typical of a TEM_{10}. Index BS5 is similar to a flat top shape with an almost constant irradiance profile, which could be represented as superimposed Gaussian and doughnut profiles, hence $TEM_{00}+TEM_{01*}$. Finally the BS6 index appears similar to a complete doughnut with TEM_{01*}.

Table 1: Beam shape indexes and their power ratios along with the measured characteristics.

Beam Shape (BS)	Power ratio (ring/core)	Closest Laguerre–Gaussian TEM	d_0 (µm)	M^2	θ (mrad)	d_0 (µm)
BS0	0/100	TEM_{00}	49	1.18	21.4	49
BS1	30/70	TEM_{00}	50	1.86	25.4	50
BS2	40/60	TEM_{10}	52	2.28	29.2	52
BS3	50/50	TEM_{10}	112	3.03	32.0	112
BS4	60/40	TEM_{10}	128	5.18	34.5	128
BS5	80/20	$TEM_{00}+TEM_{01*}$	144	5.63	38.2	144
BS6	90/10	TEM_{01*}	144	6.34	38.9	144

With the employed laser source the peak irradiance (I_{peak}) can be matched with different beam shape by means of controlling the power. It should be noted that the peak irradiance does not necessarily have to be in the beam centre for the given beam profiles. Figure 2.c depicts the irradiance profiles of BS0 and BS1 tuned to achieve the same peak irradiance at the centre. It can be seen that BS0 and BS1 at 200 W achieve 20.4 MW/cm^2 and 15 MW/cm^2 peak irradiance respectively. In order to match the same peak irradiance, the BS1 condition was tuned to 266 W empirically to produce the same peak irradiance of BS0 at 200 W. In the experimental study

all the beam shapes shown in Figure 2 were employed to assess the influence of beam shape at a fixed laser power and at a fixed peak irradiance.
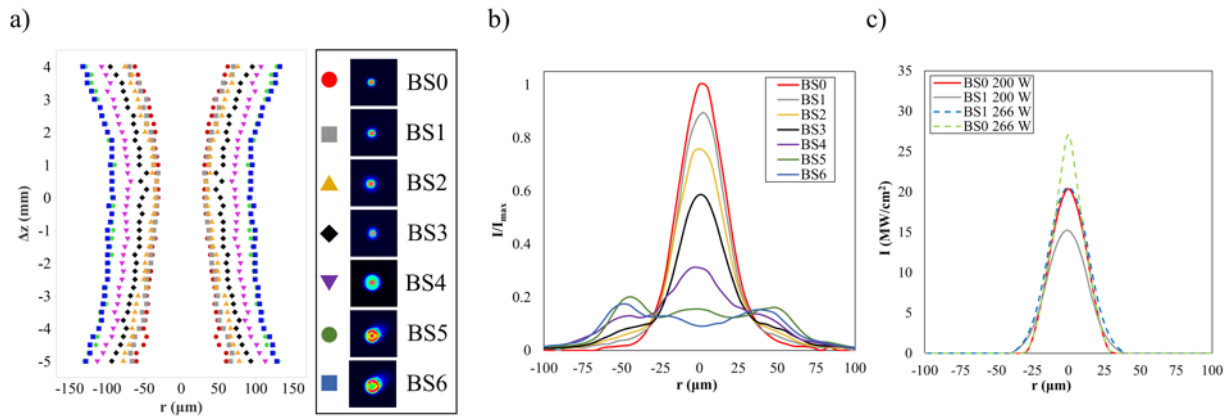

Figure 2: a) Beam propagation for the different beam indexes, b) Irradiance profiles expressed in terms of I/I_{max} at P = 200 W where I_{max} corresponds to 20.4 MW/cm², c) Beam shapes used in the experimental campaign testing the influence of the peak irradiance. Note that BS0 at 200 W and BS1 at 266 W have the same irradiance at 20.4 MW/cm².

3.2 Materials

Gas atomized AlSi7Mg0.6 with 20 and 63 μm particle size was used throughout the work (Carpenter Technology Corporation, Philadelphia, PA, USA). The measured chemical compositions was Si 9.21 ± 0.67 wt%, Mg 0.88 ± 0.19 wt%, and Al 89.91 ± 0.65 wt%. Aluminium alloy baseplates with similar chemical composition were used.

3.3 Experimental campaign

3.3.1 Densification

Prismatic samples with dimensions of 5 x 5 x 12 mm³ were built with constant hatch distance and layer thickness (h_d = 90 μm, z = 25 μm) while varying laser power (P), scan speed (v), and beam shape (BS), as shown in Table 3.

Table 2: Fixed and varied parameters used in the experimental campaign.

Fixed parameters	
Hatch distance, h_d (μm)	90
Layer thickness, z (μm)	25
Varied parameters	
Laser power, P (W)	150, 175, 200
Scan speed, v (mm/s)	500, 750, 1000
Beam shape, BS (-)	0, 1, 2, 3, 4, 5, 6

The samples were mounted, grinded, and polished. Micrographs of metallographic cross sections orthogonal to the build direction were taken with an optical microscope (Mitutoyo, QV ELF202, Kanagawa,

Japan). The images were used to measure the relative density (ρ) with an image processing software (ImageJ, U.S. National Institutes of Health, Bethesda, Maryland, USA) . The relative density ρ was estimated on the processed images with the ratio expressed in the following equation:

$$\rho \ (\%) = \left(1 - \frac{A_{pore,tot}}{A_{tot}}\right) * 100\%, \qquad\qquad 2$$

where $A_{pore,tot}$ is the total area of the pores, which corresponds to the white regions within the cross section after conversion, and A_{tot}, which is the total area of the section. Five repetitions were carried out.

3.3.2 Melt pool shape and mechanical behaviour

The experimental campaign was conducted in two sets. The first one involved variable beam shapes at a constant energy density. The condition was settled to produce specimens with adequate part density (>99.5%) through the densification study. Samples were built with constant hatch distance (h_d = 90 μm) and layer thickness (z = 25 μm), laser power (P=200 W), and scan speed (v=1000 mm/s), generating a volumetric energy density of 89 J/mm^3. The beam shape indexes available to the laser source were investigated as shown in Figure 2.a. Hatch direction was rotated by 67° between layers. Table 3 reports the experimented conditions with variable beam shapes and fixed laser power.

Table 3: Fixed and varied parameters used in the experimental campaign with fixed power.

Fixed parameters	
Hatch distance, h_d (μm)	90
Layer thickness, z (μm)	25
Laser power, P (W)	200
Scan speed, v (mm/s)	1000
Varied parameters	
Beam shape, BS (-)	0, 1, 2, 3, 4, 5, 6

In the second set, the effect of the peak irradiance at the centre and added intensity to the ring was evaluated. Beam shapes BS0 and BS1 were used as the quasi-Gaussian and quasi-Gaussian with added ring conditions respectively as shown in Figure 2.b. The peak irradiance of the BS1 at 266 W could be matched to BS0 at 200 W. Accordingly all combinations considering BS0 and BS1 with 200 W and 266 W were produced. Hatch distance, layer thickness, and scan speed were kept the same as in the first experimental set. The resultant volumetric energy densities were 89 J/mm^3 and 118 J/mm^3 for 200 W and 266 W respectively. Higher beam indexes that matched the peak irradiance of BS0 at 200 W required laser power levels exceeding the limitations of the optics, which were not included in this part of the work.

Table 4: Fixed and varied parameters used in the experimental campaign for investigating the influence of the peak irradiance and the ring irradiance.

Fixed parameters	
Hatch distance, h_d (µm)	90
Layer thickness, z (µm)	25
Scan speed, v (mm/s)	1000
Varied parameters	
Laser power, P (W)	200, 266
Beam shape, BS (-)	0, 1

Prismatic samples with dimensions of 5 mm x 5 mm x 12 mm were produced for density and melt pool geometry measurements. Cylindrical samples with ø11 mm x 70 mm were produced for tensile testing. The density (ρ) of the prismatic samples were measured using optical microscopy images of the entire cross-sections (Mitutoyo Quick Vision ELF QV-202, Kawasaki, Japan) [40]. Samples were chemically etched with Keller solution (95% H_2O, 2.5% HNO_3, 0.3% HCl, 1% HF) to reveal the microstructure. Melt pool morphology was estimated through cross-section images taken orthogonal to the build direction. The exact melt pool shape should be identified through high speed imaging [41–43] and possibly via X-ray imaging [33,44,45], which are beyond the scope of the current work. Five melt pool tracks were measured in terms of width, depth, and aspect ratio (AR=h/w) as seen in Figure 3 on the upper part of the build employing the approach reported in the works by Criales et al. [46]. Along with AR, non-dimensional *h/z* ratio was also calculated to assess the melt pool morphology and consecutive layer adhesion. The mechanical properties of the materials were tested with a tensile test machine (MTS Systems Corporation, Minneapolis, USA). The specimen geometry was designed according to ISO-6892-1 by machining cylindrical bars to the dog bone test geometry. Specimens were tested in as-built conditions without heat treatments.
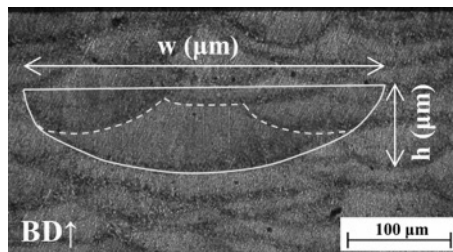

Figure 3: Melt pool width measurements taken on the micrographs (BD: Build direction).

4   Results

Figure 4 shows the samples produced with different beams shapes. It can be seen that the parts were produced free of macro defects in a stable manner for the investigated conditions. In the following sections the analysis of each investigated aspect is detailed.
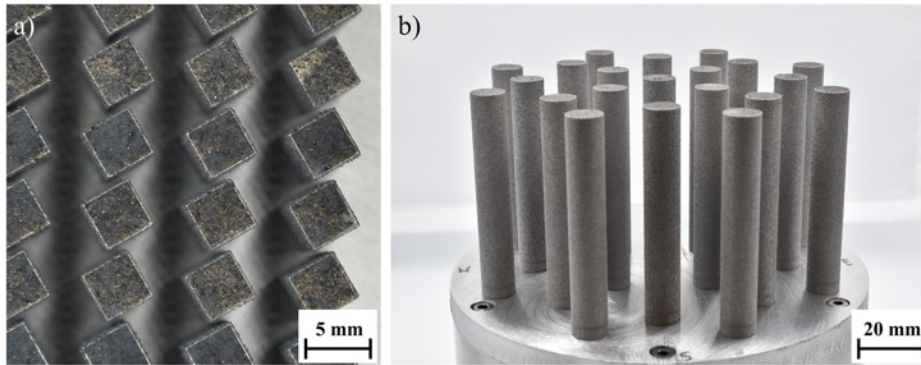

Figure 4: Examples of a) prismatic and b) cylindrical samples produced using different beam profiles.

4.1   Density

Representative metallographic cross sections obtained for the tested power levels and beam shapes with v = 1000 mm/s is shown in Figure 5. It can be seen that the decreased power in the central part of the beam requires a higher power for full densification. With fixed power at P = 150 W and v = 1000 mm/s appeared the decaying peak irradiance of the beams results in considerable lack of fusion [47]. As the the laser power is increased to P=200 W, all conditions appear to be sufficiently dense for the given speed at v = 1000 mm/s. A similar densification behaviour was observed with the slower scan speeds.
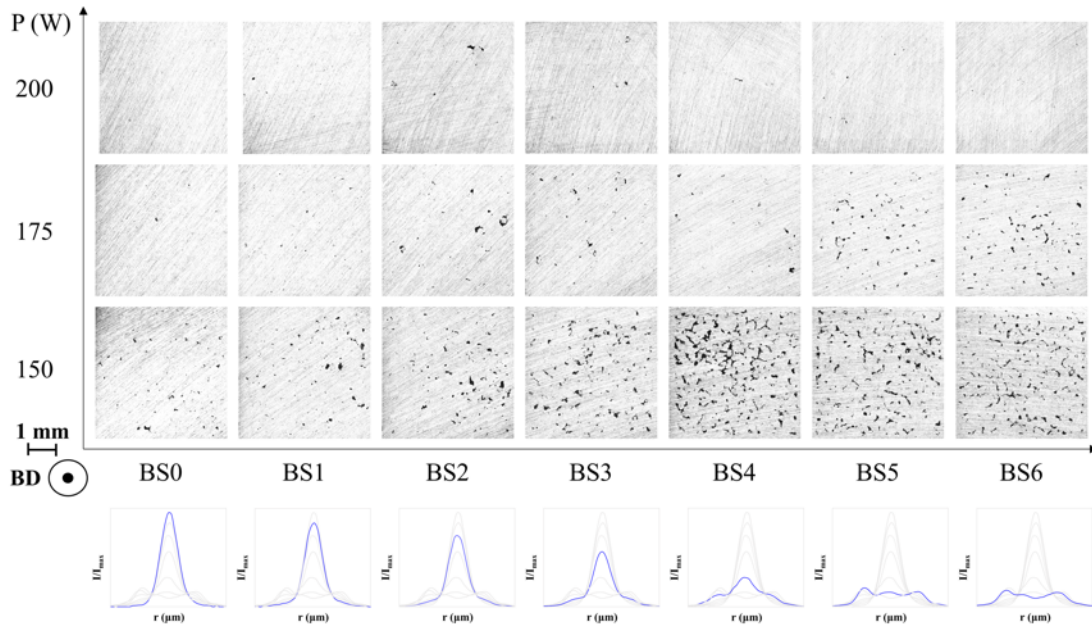
Figure 5: Metallographic cross sections comparison of various experimental conditions in terms of laser power (P) and beam shape (BS) obtained at v = 1000 mm/s (BD: Build direction).

Figure 6 shows the relative density (ρ) of the experimented conditions. It can be observed that parts with ρ > 99 % could be manufactured for each beam shape. In terms of laser power, the results depict that adequate densification could be achieved with the highest power level employed (P = 200 W). Oppositely, the effect of scan speed appeared clearly at the lowest power (P = 150 W), where ρ mostly tends to decrease with a rising scan speed. The influence of the beam profile is seen as an increase of minimum energy required for an adequate densification. While for the gaussian profile BS0, all conditions appear to be adequately dense, for the ring profile BS6 adequate densification occurs at P = 200 W. The results showed that the beam peak intensity (I) is fundamental for the correct densification as a minimum threshold is present at approximately 5 MW/cm^2, as measured from the highest intensity of the BS6 ring profile at 200 W. As a comparison, the peak intensity of the gaussian BS0 at 200 W is 20.4 MW/cm^2. In addition to the energy density, the beam intensity is expected to provide a key role in the melt pool depth and penetration to the previously melted layers. As a matter of fact, the threshold for keyhole generation is considered at an absorbed intensity of 1 MW/cm^2. With an approximately 4% optical absorption of Al, all experimented conditions are expected to be in a range of condition or conduction to keyhole transition modes.
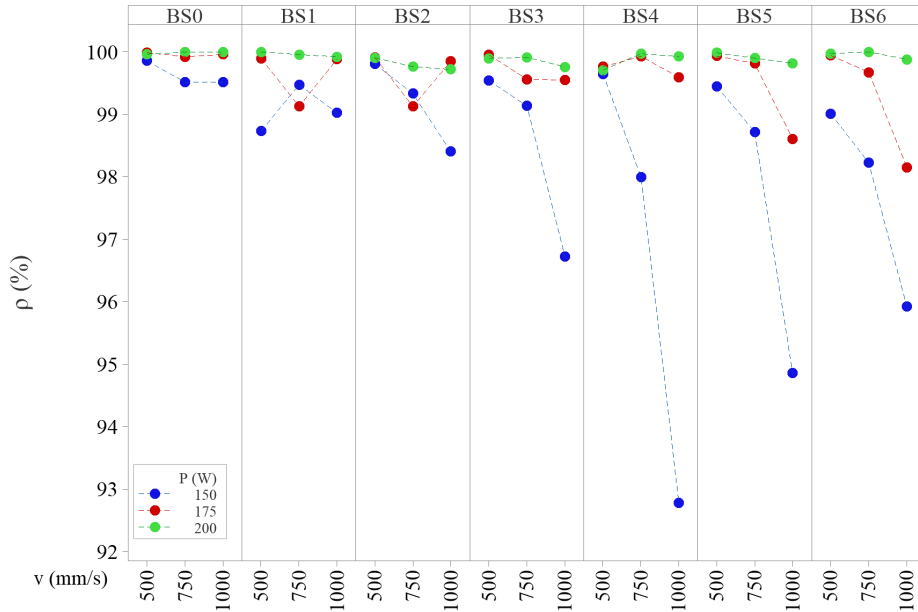
Figure 6: Density as a function of the process parameters for each beam shape.

Figure 7 shows ρ data in terms of volumetri energy density (VED) and peak irradiance (I_{peak}). Peak irradiance refers to the peak of each distribution, which lays in the origin for BS0-4 while for BS5-6 is shifted on the tails, as shown in Figure 2b. The red shaded area in Figure 7 represents a non-acceptable processing zone with ρ < 99 %. The region is indicatively delimited by the threshold 10 MW/cm² and 100 J/mm³ for irradiance and energy density, respectively. The shapes BS4-6 have the lower irradiance peaks and are more prone optical absorption variations and porosity formation. Highly dense samples with BS4-6 can be fabricated with by working with higher energy densities.
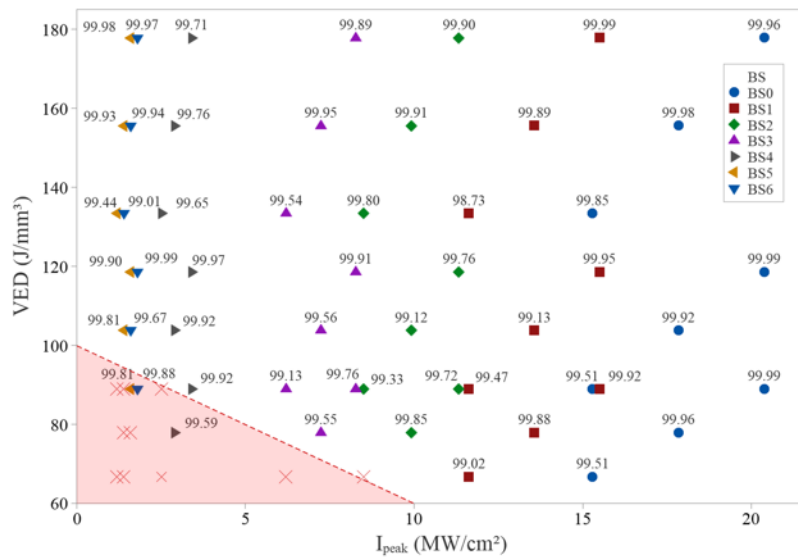
Figure 7: VED vs I_{peak} for each experimental condition. Data labels denote the correspondent ρ. Red cross symbols in the shaded area refer to ρ < 99% data.

16

4.2   Melt pool geometry

Melt pool geometry was compared in the process window where adequate density was achieved. Figure 8 shows the micrography of the specimens produced with the same power at 200 W. Chemical etching allowed to observe the typical cusp–like pattern of the melt pools generated during LPBF manufacturing [48–51]. All specimens were found to be adequately densified. On the other hand, the melt pool morphology was found to vary significantly as expected [15][27]. With an increase of the beam shape index and accordingly a decrease of the peak irradiance, the melt pool depth appears to be reduced. The melt pool width appears relatively less varied along the different conditions. Overall, the melt pools are sufficiently overlapped producing fully dense structures.
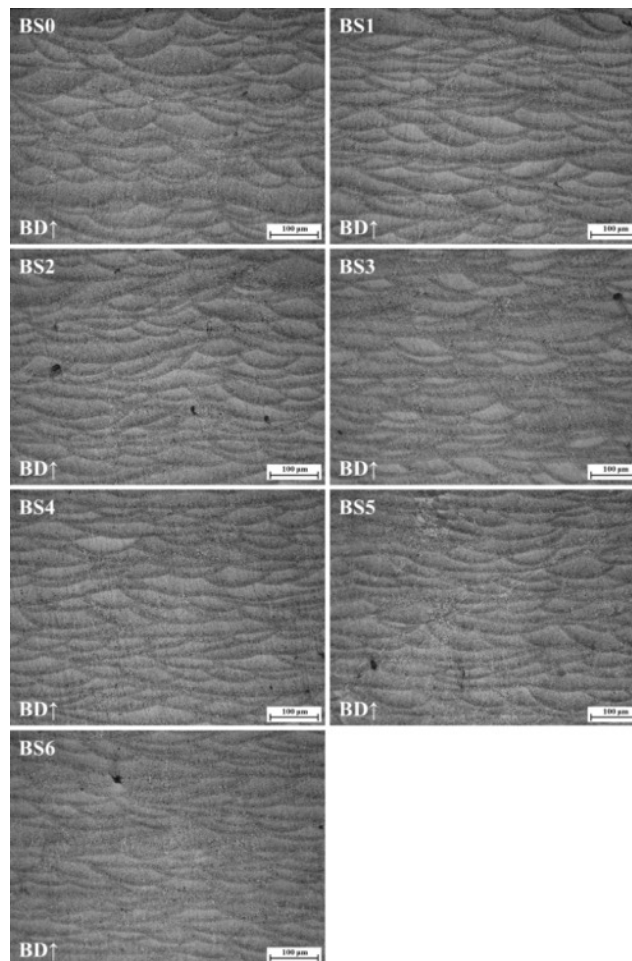
Figure 8: Cross-section images of the samples produced with different beam shapes at 200 W (BD: Build direction).

Figure 9 shows the micrographs obtained with variable power and beam shapes using BS0 and BS1. In this comparison, the influence of the peak irradiance on the melt pool remains evident. For a given beam shape a

17

higher power appears to also generate a deeper melt pool. It is interesting to see in this case that the higher peak irradiance moves the conditions towards a deeper melt pool. Moreover, at the same peak irradiance, the added power to the ring provides further increase of the melt pool depth. The melt pool width requires further attention by means of measurements for a clearer understanding.
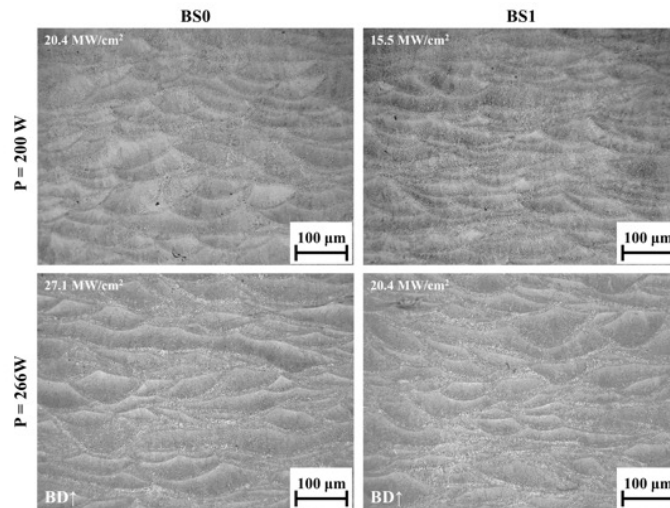

Figure 9: Cross-section images of the samples produced with BS0 and BS1 employing 200W and 266 W laser power (BD: Build direction).

Figure 10 depicts the density and the melt pool geometry measurements. In all conditions the specimens had a density over 99.5%. At 200 W, it can be seen that melt pool width shows a variable trend, remaining relatively similar between 150 and 175 µm. On the other hand, with 266 W power the width was found to be in the range of 200 µm. Concerning the melt pool depth a constant decay is observed as the beam shape index is increased at 200 W. This underlines the fact that the peak central irradiance is expected to be the main component for increasing the melt pool depth. Such observation is coherent with the overall increase of the melt pool depth at 266 W for the tested conditions. The AR measurements depict that in all the investigated conditions the process is expected to be closer to a conduction mode [47,52]. The melt pool AR is expected to be equal to or higher than 1 if keyhole based processing is present [53]. The measurements show that at 266 W a slight increase is observed with AR, where the influence of the peak influence or the laser power is yet to be resolved. The h/z index was also plotted as a means to better understand an adequate adhesion between layers. Sabzi et al. [54] and Mukherjee et al. [55] introduced an empirical condition at $h/z > 1.5$ for an adequate adhesion between layers. The h/z index, which naturally follows the same trend as melt pool depth measurements shows

that the conditions are overall all above the limit value, where the higher power conditions provide values up to 4.
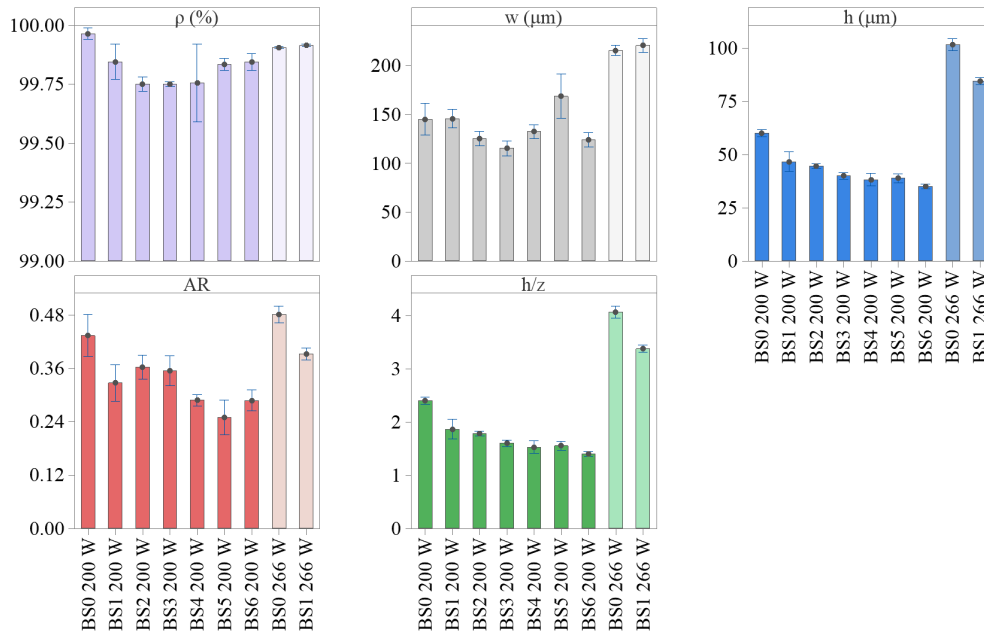

Figure 10: Specimen density and melt pool geometry measurements for the tested conditions. Lighter shaded colours indicate the higher power conditions (error bars indicate standard error).

The results were evaluated further considering the peak irradiance of each profile against the main melt pool geometry indicators AR and *h/z* as seen in Figure 11. Linear regression fits and correspondent R^2_{adj} are reported in the graphs. In all the fits the R^2_{adj} values are sufficiently high indicating adequate fitting. In the case of AR a linear trend as a function of the peak intensity was confirmed for all the employed conditions. An increasing trend of AR can be seen as a function of the peak irradiance in Figure 11.a. Such observation is coherent with the common laser melting processes, where the irradiance is conventionally manipulated by the laser power and the beam size. On the other hand, the linear trends for the *h/z* parameter were separated for the two power levels indicating the interplay between the peak irradiance and the power level (Figure 11.a.). This implies that providing more power to the ring with a fixed peak irradiance increases the penetration in a marked way.
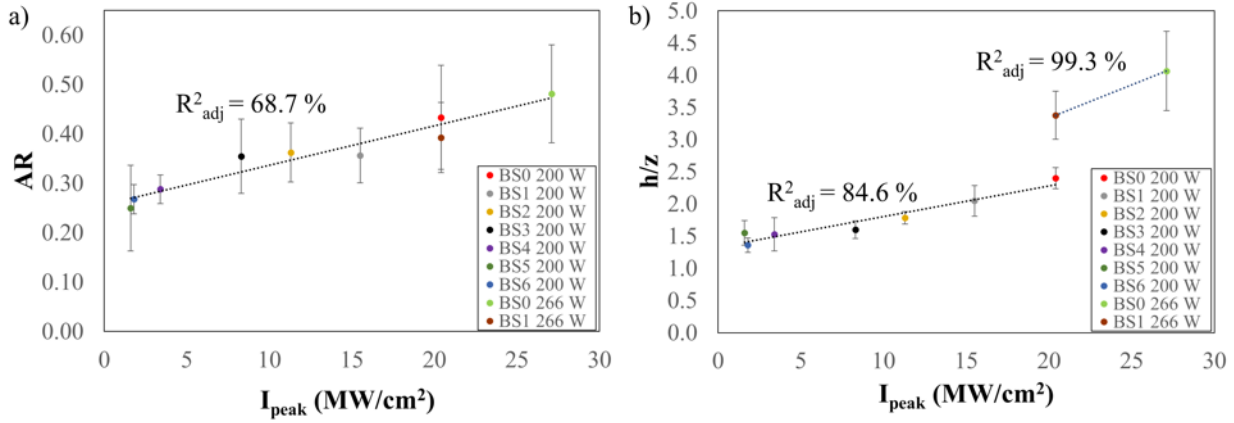
19

Figure 11: a) Aspect ratio and b) *h/z* index as a function of peak irradiance (dashed lines depict trend only).

In the light of the measurements, Figure 12 schematically compares the beam shapes and the resultant melt pool geometries for BS0 and BS1 employed with 200 W and 266 W. The schematic description helps understand the influence of the beam profile on the melt pool characteristics. It can be seen that with the same laser power and varying beam peak irradiance, the melt pool width remain similar. An increase of peak irradiance provides a higher penetration depth. Additionally, an increase of ring intensity without varying the peak irradiance (same peak irradiance with higher power) provides a deeper melt pool. The overall observations confirm that the beam shape is an effective parameter to manipulate the melt pool shape and dimensions.

An aspect worth denoting is that at constant level of peak irradiance the use of the increase of power in the ring (BS0-200 W against BS1 266 W) generates a slightly lower aspect ratio. Although, the qualitative trend reported in Figure 11 is still respected in virtue of the variability represented by the error bars, this aspect indicates that an interaction between the peak irradiance and the emission power may be significant. Further work also with the aid of numerical modelling tools to disclose the relationship correlating the melt pool morphology and peak irradiance and emission power is thus envisaged.
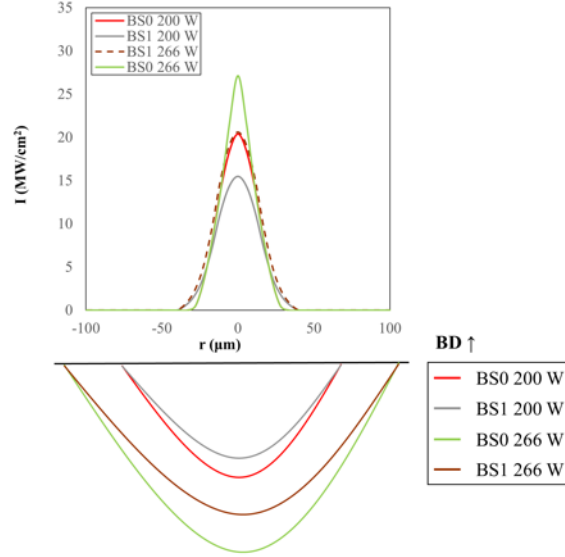
Figure 12: Schematic comparison of the melt pool shape between different irradiance profiles obtained with BS0 and BS1 using 200 and 266 W. The schematized melt pool dimensions are scaled to the beam size (BD: Build direction).

4.3 Mechanical properties

4.3.1 Influence of beam shape at fixed power and fixed peak irradiance

Table 5 summarizes the mechanical properties in terms of mean and standard deviation for each beam shape analysed at 200 W. It can be seen that the elastic modulus (E) slightly reduced with an increasing BS index. The maximum values were observed with BS0 (72 ± 3 MPa). The yield stress (YS) reduced significantly with BS index. Most of the specimens did not even reach plastic deformation. With BS0 a YS of 217 ± 4 MPa was observed whereas for the other profiles, values in the range between 180-190 MPa were obtained, while a reduction of 30 MPa occurred moving towards higher beam indexes. The ultimate tensile strength (UTS) reduced significantly with increasing BS index. With BS0 an average UTS of 344 Pa was achieved whereas for the other shapes, values in the range of 200-245 MPa were observed. The elongation at fracture (ε_f) reduced significantly with BS index. The highest elongation at fracture data were observed with BS0 specimens, with 3.8 ± 1.5 % moving towards fragile rupture with larger beam indexes. The overall results show that despite the same volumetric energy density used and the measured adequate densification the melt pool geometry is expected to have a large impact on the mechanical properties.

Table 5: Tensile properties of the LPBF specimens. E is the Young modulus, YS is the yielding strength, UTS is the ultimate tensile strength while εf is the elongation at fracture. All values are reported with average ± standard deviation values.

Condition	BS0 200W	BS1 200W	BS2 200W	BS3 200W	BS4 200W	BS5 200W	BS6 200W	BS0 266W	BS1 266W

E (GPa)	72 ± 3	69 ± 6	64 ± 5	58 ± 4	56 ± 5	58 ± 4	63 ± 1	66 ± 1	68 ± 5
YS (MPa)	217 ± 4	184 ± 54	189 ± 12	113 ± 52	184 ± 28	178 ± 6	190 ± 4	213 ± 1	216 ± 6
UTS (MPa)	344 ± 44	245 ± 55	221 ± 42	129 ± 45	202 ± 41	199 ± 14	206 ± 13	413 ± 5	362 ± 43
ε_f (%)	3.8 ± 1.5	1.4 ± 0.9	1.1 ± 0.6	0.4 ± 0.1	0.8 ± 0.3	0.8 ± 0.3	0.8 ± 0.2	9.4 ± 2.5	4.1 ± 1.2

Table 5 includes the mechanical properties of the samples obtained with 266 W with BS0 and BS1. The higher power level appears to improve the mechanical properties, especially the UTS. The highest UTS (362 ± 43 MPa) is observed with BS0 at 266 W. This condition corresponds to the highest peak irradiance and the deepest melt pool measured. The BS1 at 266 W shows a slight increase of UTS (362 ± 43 MPa) compared to that of BS0 200 W (344 ± 44 MPa). These two conditions operate at the same central peak irradiance (I_{peak}=20.4 MW/cm^2), and variable ring irradiance levels. Similar to what is observed in terms of the melt pool geometry, the mechanical properties appear to be highly influenced by the irradiance profile. In particular, the mechanical properties seem to follow a similar trend to the melt pool depth or in particular the h/z index. The only outlier in terms of mechanical properties is the condition with BS3 which yielded a significantly lower performance with respect to the other conditions tested. The loss in terms of performance appears to coincide with a smaller molten pool width which tends towards the nominal value of hatch distance. A marginally lower relative density was found for the BS3 condition which might be symptomatic of the fact that a critical condition in terms of track overlap is being approached which is known to be significantly detrimental for the mechanical performance of the material.

4.3.2 Variation of mechanical properties through the melt pool geometrical characteristics

Figure 13 collect the mechanical properties of the tested conditions. Figure 13.a and b show UTS and ε_f as a function of the h/z ratio. It can be seen that the UTS follows an asymptotic trend of improvement above 400 MPa as the h/z ratio moves towards 4.5. Consecutively the ε_f increases exponentially. As shown in Figure 13.c the resultant UTS - ε_f couples depict that the improved mechanical properties by the increased h/z index provides a stagnation over the UTS while ε_f tends to improve over higher values. Figure 13.d shows the UTS data as a function of ρ. It can be noted that the density values are varied within a very limited region with standard deviation levels similar to this variation. An attempt to verify the statistical dependence between ρ and UTS through linear regression showed a scarce fitting with R^2_{adj}=35%. Indeed, the correct densification is required for the mechanical properties, while at high density the melt pool shape is expected to play an

additional role. The deeper penetration into the previous layers can provide the improved mechanical properties. Moreover, the solidification and the grain growth directions change as a function of the melt pool shape [56], which can contribute to the higher mechanical properties in the tested direction.

In Figure 13.e, the tensile curves of the conditions with variable power (200W and 266 W) and beam shape (BS0 and BS1) are reported. The tensile curves show in detail how the irradiance tuning can be exploited to manipulate the melt pool geometry and resultantly the mechanical behaviour. It can be better viewed that the same central peak irradiance at 20.4 MW/cm^2 obtained with BS0 at 200 W and BS1 at 266 W show a similar behaviour. The condition with I_{peak}=27.1 MW/cm^2 produced with BS0 at 266 W showed a significant increase ε_f (9.4 ± 2.5) while the UTS remained similar to those achieved with I_{peak}=20.4 MW/cm^2 (BS0 at 200 W, BS1 at 266). The longer plastic deformation region of the BS0 at 266 W specimens show the importance of the high h/z factor (>4) achieved without the presence of porosity.
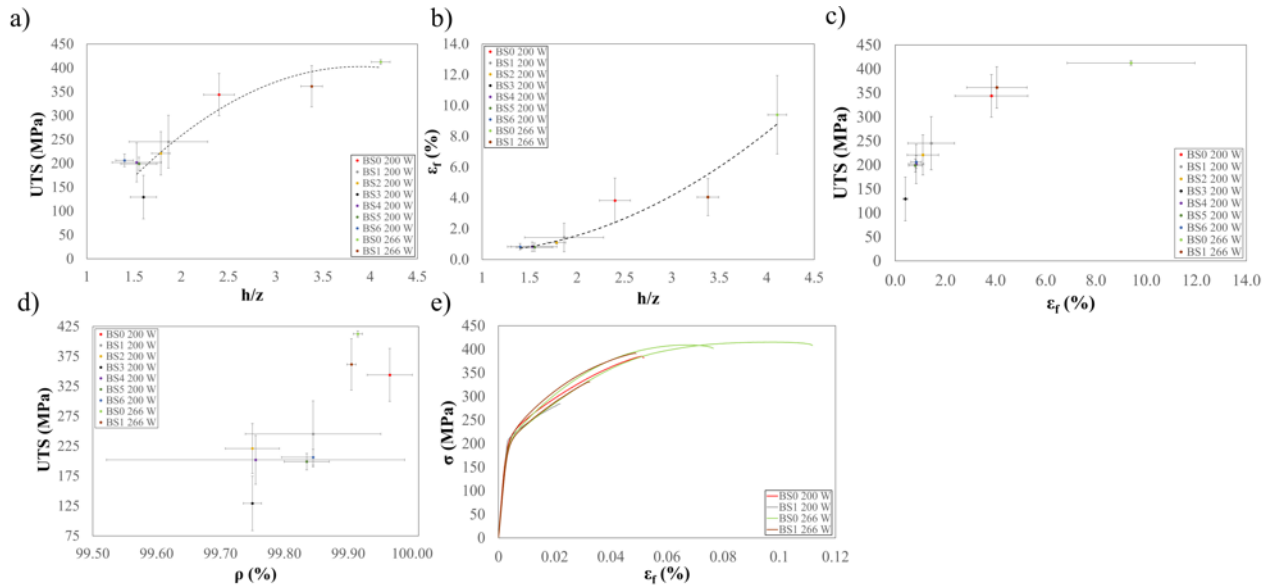
Figure 13: Mechanical properties of the specimens produced with different beam shapes and power levels. a) UTS and b) ε_f as function of the h/z ratio. c) UTS against ε_f for the tested conditions. d) UTS as a function of ρ. e) Representative tensile curves of the specimens manufactured with BS0 and BS1 at 200 W and 266 W. Error bars represent standard error and dashed lines depict trend only.

5 Discussion

The results depict that the modification of the melt pool dimensions through the irradiance profile is possible with a direct impact on the mechanical properties. The present work showed a general framework of how the possibilities to manipulate the melt pool geometry using a material with relatively low optical

absorptivity and low vaporization point. Al-alloys indeed are relatively more difficult to be processed with LPBF compared to stainless steel or Ni-alloys due to these factors. The high reflectivity of the Al-alloys require usually a high intensity beam able to overcome the superficial oxide layer and the initial reflectance by rapidly generating a molten phase [57]. The molten phase has a higher optical absorptivity, which provides a relatively easier melting process combined with the low melting point and low density of the material. In LPBF with conventional Gaussian beams an increase of the irradiance may increase the vapour fraction in the melt pool, generating a larger recoil pressure. As the recoil pressure increases, the laser beam penetrates deeper into the material. Resultantly, more laser radiance is transmitted to the material, further increasing the temperatures, the recoil pressure and the penetration. As a matter of fact the process may revert to the keyhole regime, with a pulsating keyhole [42], where gas may remain entrapped causing the circular pores typical of this condition [58]. In the experimented conditions, the peak irradiance values were not high enough to initiate keyhole formation on the processed Al-alloy. The influence of the vapour generation and recoil pressure is expected to far from initiating the keyhole. However, the recoil pressure increase is expected to depress the melt pool in the irradiated zone changing also the melt flow characteristics[59]. The results showed that the peak irradiance controlled the aspect ratio of the melt pool, while the penetration depended both on the power and the peak irradiance. It can be assumed that with the 27.4 MW/cm^2 peak irradiance a higher BS index could have provided a deeper and wider melt pool with the same aspect ratio in light of the relationship reported graphically in Figure 11.a. This condition, which could not be tested in the current experimental setup due to the limitations of the power input, can potentially provide high mechanical properties with a faster process by increasing the hatch distance. Indeed the different beam profiles can allow to manipulate the melt pool shape and potentially the microstructure [60]. Concerning the highly reflective Al-alloys, the presence of a high irradiance profile allows to increase the optical absorption with the NIR lasers through multiple reflections in a keyhole regime or a keyhole transition regime [61]. As the used ring profiles decrease the high irradiance profile, this may result in the reduction of the overall energy efficiency of the process in return.

In literature, the mechanical properties of LPBF processed materials are mostly related to the densification level. Commonly, the volumetric energy density is studied to achieve adequate density in as-built conditions, which is later on improved via the heat treatments [62]. While for materials with higher LPBF processability such as AISI 316 stainless steel, the mechanical properties in literature are often similar [34], literature shows

highly variable mechanical properties of the same AlSi7Mg0.6 alloy with different LPBF systems. The main difference can be attributed to the beam size and layer thickness values, which have a direct influence on the melt pool geometry. In conventional LPBF processes the beam irradiance is controlled through the laser power, where some systems also allow to control the beam size by defocusing units, while the layer thickness is often chosen as a compromise between productivity and feature detail. For instance, Rao et al reported UTS=396 MPa and ε_f =5% for vertical specimens produced using 30 μm layer thickness and 100 μm spot size with a build platform temperature of 35°C [63]. The same authors measured UTS=290 MPa and ε_f =3% operating with 200°C build platform [63]. Aversa et al reported UTS=426 MPa and ε_f =10% for vertical specimens produced with 30 μm layer thickness and 100 μm beam size. Denti obtained UTS=284 MPa and ε_f =7% for vertical specimens produced using a high power laser with a 400 μm beam and 50 μm layer thickness using 200°C build platform temperature [64]. Rao et al measured UTS=327 MPa and ε_f =7% employing a 100 μm beam and a 40 μm layer thickness using 200°C build platform temperature [64]. Cacace et al obtained UTS=413 MPa and ε_f =11% employing a 75 μm beam with pulsed wave emission and 25 μm layer thickness[65]. In all reported works, the process parameters were set to achieve adequate density without a particular attention on the melt pool shape. It can be expected that the large beam and high layer thickness conditions will provide lower h/z values compared to smaller beams with lower layer thicknesses. Often in these works, the LPBF process is followed by a thermal treatment to improve the mechanical properties.

The in-source dynamic beam shaping capability provided in this work can be employed to produce parts with tailored mechanical properties in a more flexible manner. On the other hand, modifications to the beam shape can affect the microstructural properties of the material in terms of texture and grain orientation functionalising the components for specific applications which will be the attention of future works. Such solutions can be used to achieve graded material properties without compromising the material density and without necessarily changing the scan strategy [64]. The successive heat treatment response can be also manipulated more freely by adjusting the melt pool size locally. The adjustment of the melt pool size can also be exploited to change the feature size locally. The fine to coarse feature adjustment can be achieved independently from the scan strategy or emission profile [66].

The current investigation intends to provide the industrial and scientific community initial information regarding a widely debated topic in literature. For the LPBF processing of Al-alloys, it appears that at equal

level of emission power tensile properties may be correlated to peak and ring irradiance levels of the laser beam together. The "irradiance tuning approach" presented in the present work, can be used as a means to maintain the mechanical properties of the material whilst providing a greater degree of freedom to manipulate the material microstructure and properties. With novel microstructures, further attention should be devoted towards the metallurgical properties of the material and the combined effect of heat treatment on the material. The present work provided some of the initial experimental data concerning novel beam shapes available to the users. Indeed, simulation based solutions will help better guide the design of the optimal irradiance profiles. Multi-physics simulations combining light propagation, temperature evolution, and fluid dynamics should be required for such purpose, where the present results can be employed also for calibration and validation.

6   Conclusions

In this work LPBF of AlSi7Mg0.6 with variable beam shapes was investigated, providing a greater understanding of the effect of different beam shapes as a relatively new topic in research. The work put together the approaches to better define non-Gaussian beam shapes by conventional irradiance parameters and an experimental study to identify the means to manipulate the melt pool size. The results confirmed the feasibility and a direct impact on the mechanical properties of the processed Al-alloy. The overall results can be summarized as follows.

- The novel multi-core fiber lasers allow to manipulate the beam shape in a dynamic way between Gaussian to doughnut shapes. The conventionally employed volumetric energy density and average irradiance may fail to describe the novel beam shapes.

- At constant volumetric energy density adequate densification (>99.5%) could be achieved with all beam shapes. However, the melt pool geometry was significantly different confirming the influence of the beam shape on the process.

- The work showed that the peak irradiance and the ring intensity should be considered together to evaluate the melt pool geometry. While the peak irradiance was found to determine the melt pool aspect ratio independently from the laser power, the melt pool depth and therefore the h/z index was influenced also by the ring intensity varied through the laser power.

- With adequately densified specimens, the mechanical properties were found to be determined by the *h/z* ratio. Hence, the beam profile was found to have a direct impact especially on the ultimate tensile strength and elongation at break.

- The results show that further irradiance tuning can improve the mechanical properties and productivity together. This could be fulfilled by adjusting the melt pool width and depth by matching the correct peak irradiance and ring intensities and increasing the hatch distance.

The results of this work provided further insights to how beam shaping in LPBF can be used to manipulate and potentially tailor the material properties. This present work aimed to provide a rigorous scientific analysis of the possibilities enabled by the use of the in-source dynamic beam shaping architecture of latest generation laser sources without the intention to single out a superior new beam shape. Although at equal level of emission power higher ultimate tensile stress and ductility were exhibited by the material deposited with the Gaussian beam, different microstructural aspects and texture may yield a positive effect over different directions. Indeed for a better exploitation the experimental efforts should be accompanied by modelling to better navigate in a multi-dimensional parameter space. From this perspective ray-tracing methods in finite element modelling approaches will be essential. Further attention should be also paid to the material characterization from a more detailed analysis perspective, investigating the influence of the thermal field and the melt pool shape on the grain growth and phases generated.

Authorship contribution statement

Francesco Galbusera: Conceptualization, Formal analysis, Investigation, Data curation, Software, Writing - original draft, Writing - review & editing. **Leonardo Caprio**: Methodology, Writing - original draft, Writing - review & editing. **Barbara Previtali**: Methodology, Supervision, Resources, Writing - original draft, Writing - review & editing. **Ali Gökhan Demir**: Conceptualization, Methodology, Supervision, Formal analysis, Investigation, Writing - original draft, Writing - review & editing.

Acknowledgements

References

[1] Demir AG, Colombo P, Previtali B. From pulsed to continuous wave emission in SLM with contemporary fiber laser sources: effect of temporal and spatial pulse overlap in part quality. Int J Adv Manuf Technol 2017;91:2701–14. doi:10.1007/s00170-016-9948-7.

[2] Shi W, Schulzgen A, Amezcua R, Zhu X, Alam S-U. Fiber lasers and their applications: introduction. J Opt Soc Am B 2017;34:FLA1. doi:10.1364/josab.34.00fla1.

[3] Kang SG, Shin J. Laser beam oscillation welding of aluminum alloy using the spatially modulated beam by diffractive optical element (DOE). J Manuf Process 2021;66:387–96. doi:10.1016/j.jmapro.2021.04.029.

[4] Yuan R, Deng S, Cui H, Chen Y, Lu F. Interface characterization and mechanical properties of dual beam laser welding-brazing Al/steel dissimilar metals. J Manuf Process 2019;40:37–45. doi:10.1016/j.jmapro.2019.03.005.

[5] Laskin A, Volpp J, Laskin V, Nara T, Jung SR. Multispot optics for beam shaping of high-power single-mode and multimode lasers. J Laser Appl 2021;33:042046. doi:10.2351/7.0000461.

[6] Shusteff M, Browar AEM, Kelly BE, Henriksson J, Weisgraber TH, Panas RM, et al. One-step volumetric additive manufacturing of complex polymer structures. Sci Adv 2017;3. doi:10.1126/sciadv.aao5496.

[7] Zavala-Arredondo M, Boone N, Willmott J, Childs DTD, Ivanov P, Groom KM, et al. Laser diode area melting for high speed additive manufacturing of metallic components. Mater Des 2017;117:305–15. doi:10.1016/j.matdes.2016.12.095.

[8] Mi Y, Mahade S, Sikström F, Choquet I, Joshi S, Ancona A. Conduction mode laser welding with beam shaping using a deformable mirror. Opt Laser Technol 2022;148. doi:10.1016/j.optlastec.2021.107718.

[9] Hansen KS, Kristiansen M, Olsen FO. Beam shaping to control of weldpool size in width and depth. Phys Procedia 2014;56:467–76. doi:10.1016/j.phpro.2014.08.150.

[10] Tenbrock C, Fischer FG, Wissenbach K, Schleifenbaum JH, Wagenblast P, Meiners W, et al. Influence

of keyhole and conduction mode melting for top-hat shaped beam profiles in laser powder bed fusion. J Mater Process Technol 2020;278:116514. doi:10.1016/j.jmatprotec.2019.116514.

[11]   Victor B, Kliner D, Hepp M. Is beam shaping the future of laser welding? 2019:9–12.

[12]   Wang L, Mohammadpour M, Gao X, Lavoie JP, Kleine K, Kong F, et al. Adjustable Ring Mode (ARM) laser welding of stainless steels. Opt Lasers Eng 2021;137. doi:10.1016/j.optlaseng.2020.106360.

[13]   Wang L, Gao X, Kong F. Keyhole dynamic status and spatter behavior during welding of stainless steel with adjustable-ring mode laser beam. J Manuf Process 2022;74:201–19. doi:10.1016/j.jmapro.2021.12.011.

[14]   Li Q, Luo M, Mu Z, Huang A, Pang S. Improving laser welding via decreasing central beam density with a hollow beam. J Manuf Process 2022;73:939–47. doi:10.1016/j.jmapro.2021.12.001.

[15]   Roehling TT, Shi R, Khairallah SA, Roehling JD, Guss GM, McKeown JT, et al. Controlling grain nucleation and morphology by laser beam shaping in metal additive manufacturing. Mater Des 2020;195:109071. doi:10.1016/j.matdes.2020.109071.

[16]   Matthews MJ, Roehling TT, Khairallah SA, Guss G, Wu SQ, Crumb MF, et al. Spatial modulation of laser sources for microstructural control of additively manufactured metals. Procedia CIRP 2018;74:607–10. doi:10.1016/j.procir.2018.08.077.

[17]   Shi R, Khairallah SA, Roehling TT, Heo TW, McKeown JT, Matthews MJ. Microstructural control in metal laser powder bed fusion additive manufacturing using laser beam shaping strategy. Acta Mater 2020;184:284–305. doi:10.1016/j.actamat.2019.11.053.

[18]   Tumkur TU, Voisin T, Shi R, Depond PJ, Roehling TT, Wu S, et al. Nondiffractive beam shaping for enhanced optothermal control in metal additive manufacturing. Sci Adv 2021;7:1–12. doi:10.1126/sciadv.abg9358.

[19]   Cloots M, Uggowitzer PJ, Wegener K. Investigations on the microstructure and crack formation of IN738LC samples processed by selective laser melting using Gaussian and doughnut profiles. Mater Des 2016;89:770–84. doi:10.1016/j.matdes.2015.10.027.

[20] Wischeropp TM, Tarhini H, Emmelmann C. Influence of laser beam profile on the selective laser melting process of AlSi10Mg. J Laser Appl 2020;32:022059. doi:10.2351/7.0000100.

[21] Schleifenbaum H, Meiners W, Wissenbach K, Hinke C. High power selective laser melting: A new approach for individualized series production. ICALEO 2009 - 28th Int Congr Appl Lasers Electro-Optics, Congr Proc 2009;102:385–94. doi:10.2351/1.5061585.

[22] Zhirnov I V., Podrabinnik PA, Okunkova AA, Gusarov A V. Laser beam profiling: Experimental study of its influence on single-track formation by selective laser melting. Mech Ind 2015;16. doi:10.1051/meca/2015082.

[23] Metel A, Stebulyanin M, Fedorov S, Okunkova A. Power Density Distribution for Laser Additive Manufacturing (SLM): Potential, Fundamentals and Advanced Applications. Technologies 2018;7:5. doi:10.3390/technologies7010005.

[24] Okunkova AA, Peretyagin PY, Podrabinnik PA, Zhirnov I V., Gusarov A V. Development of Laser Beam Modulation Assets for the Process Productivity Improvement of Selective Laser Melting. Procedia IUTAM 2017;23:177–86. doi:10.1016/j.piutam.2017.06.019.

[25] Liu M, Wei K, Yue X, Huang G, Deng J, Zeng X. High power laser powder bed fusion of AlSi10Mg alloy_ Effect of laser beam mode. J Alloys Compd 2022;909:164779. doi:10.1016/j.jallcom.2022.164779.

[26] Loh LE, Liu ZH, Zhang DQ, Mapar M, Sing SL, Chua CK, et al. Selective Laser Melting of aluminium alloy using a uniform beam profile. Virtual Phys Prototyp 2014;9:11–6. doi:10.1080/17452759.2013.869608.

[27] Grünewald J, Gehringer F, Schmöller M, Wudy K. Influence of ring-shaped beam profiles on process stability and productivity in laser-based powder bed fusion of AISI 316L. Metals (Basel) 2021;11:1–18. doi:10.3390/met11121989.

[28] Grünewald J, Blickle V, Allenberg-Rabe M, Wagenblast P, Wudy K. Flexible and highly dynamic beam shaping for Laser-Based Powder Bed Fusion of metals. Procedia CIRP 2022;111:65–70. doi:10.1016/j.procir.2022.08.124.

[29] nLIGHT Inc. AFX User Manual Single-mode Fiber Laser with Programmable Beam Shaping 2020.

[30] Kotadia HR, Gibbons G, Das A, Howes PD. A review of Laser Powder Bed Fusion Additive Manufacturing of aluminium alloys: Microstructure and properties. Addit Manuf 2021;46:102155. doi:10.1016/j.addma.2021.102155.

[31] Olakanmi EO, Cochrane RF, Dalgarno KW. A review on selective laser sintering/melting (SLS/SLM) of aluminium alloy powders: Processing, microstructure, and properties. Prog Mater Sci 2015;74:401–77. doi:10.1016/j.pmatsci.2015.03.002.

[32] Fiocchi J, Tuissi A, Biffi CA. Heat treatment of aluminium alloys produced by laser powder bed fusion: A review. Mater Des 2021;204. doi:10.1016/j.matdes.2021.109651.

[33] Cunningham R, Zhao C, Parab N, Kantzos C, Pauza J, Fezzaa K, et al. Keyhole threshold and morphology in laser melting revealed by ultrahigh-speed x-ray imaging. Science (80-) 2019;363:849–52. doi:10.1126/science.aav4687.

[34] Fayazfar H, Salarian M, Rogalsky A, Sarker D, Russo P, Paserin V, et al. A critical review of powder-based additive manufacturing of ferrous alloys: Process parameters, microstructure and mechanical properties. Mater Des 2018;144:98–128. doi:10.1016/j.matdes.2018.02.018.

[35] Steen WM, Mazumder J. Laser Material Processing. London: Springer London; 2010. doi:10.1007/978-1-84996-062-5.

[36] Liu JM. Simple technique for measurements of pulsed Gaussian-beam spot sizes. Opt Lett 1982;7:196. doi:10.1364/OL.7.000196.

[37] Assuncao E, Williams S, Yapp D. Interaction time and beam diameter effects on the conduction mode limit. Opt Lasers Eng 2012;50:823–8. doi:10.1016/j.optlaseng.2012.02.001.

[38] Demir AG, Pangovski K, O'Neill W, Previtali B. Laser micromachining of TiN coatings with variable pulse durations and shapes in ns regime. Surf Coatings Technol 2014;258:240–8. doi:10.1016/j.surfcoat.2014.09.021.

[39] Ahmmed KMT, Ling EJY, Servio P, Kietzig A-M. Introducing a new optimization tool for femtosecond

laser-induced surface texturing on titanium, stainless steel, aluminum and copper. Opt Lasers Eng 2015;66:258–68. doi:10.1016/j.optlaseng.2014.09.017.

[40]   Spierings AB, Schneider M, Eggenberger R. Comparison of density measurement techniques for additive manufactured metallic parts. Rapid Prototyp J 2011;17:380–6. doi:10.1108/13552541111156504.

[41]   Pacher M, Mazzoleni L, Caprio L, Demir AG, Previtali B. Estimation of melt pool size by complementary use of external illumination and process emission in coaxial monitoring of selective laser melting. J Laser Appl 2019;31:022305. doi:10.2351/1.5096117.

[42]   Caprio L, Demir AG, Previtali B. Observing molten pool surface oscillations during keyhole processing in laser powder bed fusion as a novel method to estimate the penetration depth. Addit Manuf 2020:101470. doi:10.1016/j.addma.2020.101470.

[43]   Caprio L, Demir AG, Previtali B. External Illumination Enables Coaxial Sensing of Surface and Subsurface Molten Pool Geometry in LPBF. Metals (Basel) 2022;12:1762. doi:10.3390/met12101762.

[44]   Calta NP, Wang J, Kiss AM, Martin AA, Depond PJ, Guss GM, et al. An instrument for in situ time-resolved X-ray imaging and diffraction of laser powder bed fusion additive manufacturing processes. Rev Sci Instrum 2018;89. doi:10.1063/1.5017236.

[45]   Parab ND, Zhao C, Cunningham R, Escano LI, Fezzaa K, Everhart W, et al. Ultrafast X-ray imaging of laser–metal additive manufacturing processes. J Synchrotron Radiat 2018;25:1–11. doi:10.1107/S1600577518009554.

[46]   Criales LE, Arısoy YM, Lane B, Moylan S, Donmez A, Özel T. Laser powder bed fusion of nickel alloy 625: Experimental investigations of effects of process parameters on melt pool size and shape with spatter analysis. Int J Mach Tools Manuf 2017;121:22–36. doi:10.1016/j.ijmachtools.2017.03.004.

[47]   Cunningham R, Narra SP, Rollett AD. Synchrotron-Based X-ray Microtomography Characterization of the Effect of Processing Variables on Porosity Formation in Laser Power-Bed Additive Manufacturing of Ti-6Al-4V Synchrotron-Based X-Ray Microtomography Characterization of the

Effect of Processin 2017. doi:10.1007/s11837-016-2234-1.

[48]   Weingarten C, Buchbinder D, Pirch N, Meiners W, Wissenbach K, Poprawe R. Formation and reduction of hydrogen porosity during selective laser melting of AlSi10Mg. J Mater Process Technol 2015;221:112–20. doi:10.1016/j.jmatprotec.2015.02.013.

[49]   Thijs L, Kempen K, Kruth JP, Van Humbeeck J. Fine-structured aluminium products with controllable texture by selective laser melting of pre-alloyed AlSi10Mg powder. Acta Mater 2013;61:1809–19. doi:10.1016/j.actamat.2012.11.052.

[50]   Chou R, Ghosh A, Chou SC, Paliwal M, Brochu M. Microstructure and mechanical properties of Al10SiMg fabricated by pulsed laser powder bed fusion. Mater Sci Eng A 2017;689:53–62. doi:10.1016/j.msea.2017.02.023.

[51]   Qin H, Fallah V, Dong Q, Brochu M, Daymond MR, Gallerneault M. Solidification pattern, microstructure and texture development in Laser Powder Bed Fusion (LPBF) of Al10SiMg alloy. Mater Charact 2018;145:29–38. doi:10.1016/j.matchar.2018.08.025.

[52]   Fabbro R. Depth dependence and keyhole stability at threshold, for different laser welding regimes. Appl Sci 2020;10. doi:10.3390/app10041487.

[53]   King WE, Barth HD, Castillo VM, Gallegos GF, Gibbs JW, Hahn DE, et al. Observation of keyhole-mode laser melting in laser powder-bed fusion additive manufacturing. J Mater Process Technol 2014;214:2915–25. doi:10.1016/j.jmatprotec.2014.06.005.

[54]   Sabzi HE, Rivera-Díaz-del-Castillo PEJ. Defect prevention in selective laser melting components: Compositional and process effects. Materials (Basel) 2019;12. doi:10.3390/ma12223791.

[55]   Mukherjee T, Zuback JS, De A, DebRoy T. Printability of alloys for additive manufacturing. Sci Rep 2016;6:1–8. doi:10.1038/srep19717.

[56]   Pérez-Ruiz JD, de Lacalle LNL, Urbikain G, Pereira O, Martínez S, Bris J. On the relationship between cutting forces and anisotropy features in the milling of LPBF Inconel 718 for near net shape parts. Int J Mach Tools Manuf 2021;170. doi:10.1016/j.ijmachtools.2021.103801.

[57]   Louvis E, Fox P, Sutcliffe CJ. Selective laser melting of aluminium components. J Mater Process Technol 2011;211:275–84. doi:10.1016/j.jmatprotec.2010.09.019.

[58]   Zhao C, Parab ND, Li X, Fezzaa K, Tan W, Rollett AD, et al. Critical instability at moving keyhole tip generates porosity in laser melting. Science (80-) 2020;370:1080–6. doi:10.1126/science.abd1587.

[59]   Simonds BJ, Tanner J, Artusio-Glimpse A, Williams PA, Parab N, Zhao C, et al. The causal relationship between melt pool geometry and energy absorption measured in real time during laser-based manufacturing. Appl Mater Today 2021;23:101049. doi:10.1016/j.apmt.2021.101049.

[60]   Han J, Shi Y, Zhang G, Volodymyr K, Le W yun. Minimizing defects and controlling the morphology of laser welded aluminum alloys using power modulation-based laser beam oscillation. J Manuf Process 2022;83:49–59. doi:10.1016/j.jmapro.2022.08.031.

[61]   Kim H, Nam K, Kim Y, Ki H. Analysis of laser-beam absorptance and keyhole behavior during laser keyhole welding of aluminum alloy using a deep-learning-based monitoring system. J Manuf Process 2022;80:75–86. doi:10.1016/j.jmapro.2022.05.044.

[62]   Yang K V., Rometsch P, Davies CHJ, Huang A, Wu X. Effect of heat treatment on the microstructure and anisotropy in mechanical properties of A357 alloy produced by selective laser melting. Mater Des 2018;154:275–90. doi:10.1016/j.matdes.2018.05.026.

[63]   Rao H, Giet S, Yang K, Wu X, Davies CHJ. The influence of processing parameters on aluminium alloy A357 manufactured by Selective Laser Melting. Mater Des 2016;109:334–46. doi:10.1016/j.matdes.2016.07.009.

[64]   Denti L. Additive manufactured A357.0 samples using the laser powder bed fusion technique: Shear and tensile performance. Metals (Basel) 2018;8. doi:10.3390/met8090670.

[65]   Cacace S, Gökhan Demir A, Sala G, Mattia Grande A. Influence of production batch related parameters on static and fatigue resistance of LPBF produced AlSi7Mg0.6. Int J Fatigue 2022;165:0–11. doi:10.1016/j.ijfatigue.2022.107227.

[66]   Demir AG, Mazzoleni L, Caprio L, Pacher M, Previtali B. Complementary use of pulsed and

continuous wave emission modes to stabilize melt pool geometry in laser powder bed fusion. Opt Laser

Technol 2019;113. doi:10.1016/j.optlastec.2018.12.005.

List of tables

List of figures